Energy Flux and Dissipation in Luzon Strait: Two Tales of Two Ridges

MATTHEW H. ALFORD,* JENNIFER A. MACKINNON,+ JONATHAN D. NASH,# HARPER SIMMONS,@ ANDY PICKERING,* JODY M. KLYMAK,& ROBERT PINKEL,+ OLIVER SUN,+ LUC RAINVILLE,* RUTH MUSGRAVE,+ TAMARA BEITZEL,+ KE-HSIEN FU,** AND CHUNG-WEI LU**

* *Applied Physics Laboratory, and School of Oceanography, University of Washington, Seattle, Washington*
+ *Scripps Institution of Oceanography, University of California, San Diego, La Jolla, California*
# *College of Ocean and Atmospheric Science, Oregon State University, Corvallis, Oregon*
@ *University of Alaska Fairbanks, Fairbanks, Alaska*
& *School of Earth and Ocean Sciences, University of Victoria, Victoria, British Columbia, Canada*
** *National Sun-Yat Sen University, Kaohsiung, Taiwan*

(Manuscript received 23 March 2011, in final form 27 June 2011)

ABSTRACT

Internal tide generation, propagation, and dissipation are investigated in Luzon Strait, a system of two quasi-parallel ridges situated between Taiwan and the Philippines. Two profiling moorings deployed for about 20 days and a set of nineteen 36-h lowered ADCP–CTD time series stations allowed separate measurement of diurnal and semidiurnal internal tide signals. Measurements were concentrated on a northern line, where the ridge spacing was approximately equal to the mode-1 wavelength for semidiurnal motions, and a southern line, where the spacing was approximately two-thirds that. The authors contrast the two sites to emphasize the potential importance of resonance between generation sites. Throughout Luzon Strait, baroclinic energy, energy fluxes, and turbulent dissipation were some of the strongest ever measured. Peak-to-peak baroclinic velocity and vertical displacements often exceeded 2 m s^{-1} and 300 m, respectively. Energy fluxes exceeding 60 kW m^{-1} were measured at spring tide at the western end of the southern line. On the northern line, where the western ridge generates appreciable eastward-moving signals, net energy flux between the ridges was much smaller, exhibiting a nearly standing wave pattern. Overturns tens to hundreds of meters high were observed at almost all stations. Associated dissipation was elevated in the bottom 500–1000 m but was strongest by far atop the western ridge on the northern line, where >500-m overturns resulted in dissipation exceeding 2×10^{-6} W kg^{-1} (implying diapycnal diffusivity $K_\rho > 0.2$ m^2 s^{-1}). Integrated dissipation at this location is comparable to conversion and flux divergence terms in the energy budget. The authors speculate that resonance between the two ridges may partly explain the energetic motions and heightened dissipation.

1. Introduction

Internal tides are thought to provide a substantial portion of the power available to mix the abyssal ocean. Generated by barotropic tidal flow over undersea topography, a fraction of the energy lost to the barotropic tide is dissipated locally, whereas the rest escapes into low-mode motions that can propagate far away from the generation region. The fraction, q, of the total barotropic conversion lost to local dissipation is set by a range of processes including generation of tidal ''beams'' (Cole et al. 2009), nonlinear interactions (St. Laurent and Garrett 2002; Polzin 2004; Nikurashin and Legg 2011), convective instability over steep slopes, and high-mode hydraulically controlled features (Klymak et al. 2008; Klymak and Legg 2010). Determination of q for a broad range of topography is a key step toward improving numerical circulation models, because they depend sensitively on both the magnitude and distribution of internal tide mixing (Simmons et al. 2004a). At geographically isolated supercritical topography such as the Hawaiian Ridge, the locally dissipated fraction q appears to be small, because of the predominant generation of quasi-linear low-mode waves.

However, in much of the ocean, the generation story is complicated by complex topography, which produces interference between waves from multiple generation sources in close proximity. At a minimum, such superposition leads to confusing patterns of wave kinematics and energy fluxes (exhibiting, e.g., fluxes pointing transverse to

Corresponding author address: Matthew H. Alford, Applied Physics Laboratory, 1013 NE 40th St., Seattle, WA 98105.
E-mail: malford@apl.washington.edu

DOI: 10.1175/JPO-D-11-073.1

true propagation directions; Rainville et al. 2010; Zhao et al. 2010). Furthermore, the detailed phasing between multiple waves can affect wave scattering and transmission at topographic boundaries (Klymak et al. 2011). More troublesome is the recent finding (Kelly and Nash 2010) that interference between incident baroclinic waves and local barotropic forcing can fundamentally alter the nature and magnitude of local barotropic to baroclinic conversion.

A concrete example of this situation is barotropic tidal flow past two supercritical ridges, where generation at each depends sensitively on waves generated at the other. In physics analogous to the situation described by Kelly and Nash (2010), generation in a two-ridge system depends on the ridge spacing relative to the internal tide wavelength at a particular forcing frequency. For ridge separations that are multiples of the baroclinic tidal wavelength, resonance can occur, with significant baroclinic energy amplification (Echeverri and Peacock 2010; Tang and Peacock 2010). One ultimate goal of the current research is to understand how integrated parameters like local dissipation, conversion, and the ratio of the two (q) change in such complex topography.

Luzon Strait, a two-ridge system between Taiwan and the Philippines island of Luzon (Fig. 1), provides an excellent laboratory to test some of these questions, not only because of its extremely vigorous tides but also the variations in geometry in the north–south direction. Specifically, the spacing between the ridges varies appreciably from nearly resonant for semidiurnal motions near 20.6°N (Fig. 2, top right; gray semidiurnal characteristics nearly connecting the two ridge tops) to nonresonant farther south (Fig. 2, bottom right) and at both locations for the diurnal motions (Fig. 2, left). Results presented here are from a series of measurements conducted in boreal summer 2010 as part of the Internal Waves in Straits Experiment, a multiyear initiative funded by the Office of Naval Research. Stations and moorings deployed along two cross-ridge lines allowed us to compute dissipation, energy, and energy flux separately for the semidiurnal and diurnal components of the flow, which is important because their different wavelengths allow for the possibility of resonance for one constituent but not the other.

2. Measurements and techniques

Data are from two cruises, which took place between 19 June and 2 July 2010 and between 14 August and 12 September 2010. The general strategy in both cruises was to occupy a series of lowered ADCP (LADCP)–CTD stations, with each lasting 36 h, along the two cross-ridge lines shown in Fig. 1. Every 1–2 h (depending on the water depth), an up–down cycle from 10-m depth to about 10 m above the bottom was completed. Full-depth velocity was measured with two 300-KHz ADCPs affixed to the CTD rosette frame, with one looking upward and one looking downward. These were processed following standard LADCP processing techniques (Thurnherr 2010). Potential density from the CTD was then used to compute isopycnal displacements η relative to the 36-h station-mean potential density profile. Baroclinic pressure was then computed from full-depth density profiles assuming hydrostaticity (Althaus et al. 2003; Nash et al. 2005).

Potential density data were also used to compute overturns from Thorpe scales (Thorpe 1977; Dillon 1982; Ferron et al. 1998; Alford et al. 2006a), giving estimates of turbulent dissipation rate ϵ and diapycnal diffusivity $K_\rho = \Gamma\epsilon/\overline{N^2}$ (Osborn 1980), where $\Gamma = 0.2$ is the mixing efficiency and $\overline{N^2}$ is the average buoyancy gradient.

Data were decomposed into their mean, diurnal, and semidiurnal components by harmonic analysis of the time series of u, v, and η at each depth. Because 36-h stations do not allow separation of the K_1/O_1 and M_2/S_2 tidal constituents, we refer to these as D_1 and D_2, respectively. Energy flux is computed in each band at each station following Nash et al. (2005). Though cross-terms can potentially complicate separation of energy flux constituents from short time series, in our data the total flux measured without harmonic fits nearly equals the sum of the D_2 and D_1 components.

Barotropic forcing varies substantially over the period of our observations as the M_2, S_2, K_1, and O_1 components beat together, as demonstrated by predictions from the Oregon State TOPEX/Poseidon Global Inverse Solution (TPXO6.2) (Egbert and Erofeeva 2002) evaluated over the eastern ridge at latitude 21° (Fig. 3a). TPXO6.2 is used instead of the more recent version 7.2 because Ramp et al. (2010) found that it agreed better with observed currents. The amplitude of the diurnal and semidiurnal forcing, calculated by computing harmonic fits to this time series in 3-day windows, is overplotted (blue and red, respectively). The phasing and amplitude of the K_1 and O_1 constituents are such that the diurnal barotropic velocities are nearly zero at diurnal neap (year days 226 and 240), increasing to 0.26 m s^{-1} at spring. The modulation of the semidiurnal forcing is more moderate.

The time of each station is indicated in Fig. 3a. Because we were interested in examining the differences between predominantly diurnally forced periods (e.g., yearday 232) and semidiurnal periods, when possible we reoccupied stations at both phases (e.g., stations S6a, S6b, N2a, and N2b). Measured barotropic velocities at each station (colored lines) confirm the phasing of the TPXO6.2 predictions, as found by Alford et al. (2010) and Ramp et al. (2010). Amplitudes are in reasonable agreement as well, particularly on the northern line and the shallower southern-line stations (e.g., S5). Observed currents are weaker than modeled at the deep southern

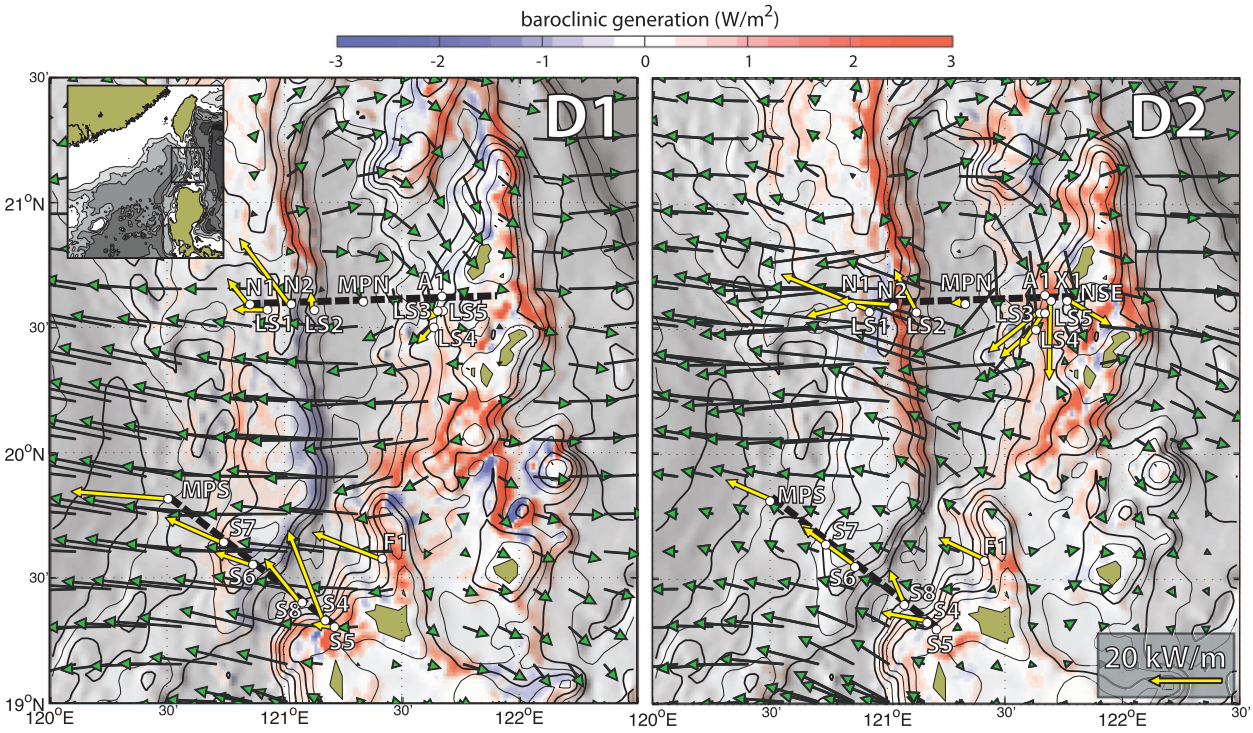

FIG. 1. Conversion (colors) and baroclinic energy flux (thin arrows) from a 3D 2.5-km isopycnal-coordinate numerical simulation (H. Simmons et al. 2011, unpublished manuscript) for the (left) diurnal and (right) semidiurnal constituents. The two lines occupied are shown with dashed lines. Stations and measured energy flux are overplotted (white dots and yellow arrows). The reference arrow for flux is shown at the bottom right. Model conversion and fluxes are separated into diurnal and semidiurnal components by bandpassing, whereas observed fluxes are computed by harmonic analysis at each 36-h station. All energy flux values are synoptic (corrected for sample time within spring–neap cycle; see text and Table 1). For clarity, model fluxes are plotted only at every 16th model grid point. (top left) The inset shows the larger region.

stations, as expected because the model barotropic currents are taken at a shallow location on the eastern ridge.

Two profiling moorings were deployed for most of the duration of the second cruise, in the center of the northern line (MPN; 21 days) and west of the western ridge on the southern line (MPS; 16 days). Though the records are modest in length compared to typical mooring deployments, they allow contextualization of the short LADCP–CTD stations with respect to the spring–neap forcing cycle. Because the design of the two moorings was similar, data from MPN are used to illustrate their depth coverage, performance, and basic aspects of the data (Figs. 3b,c). Each mooring consisted of a subsurface float at a nominal depth of 80 m housing an upward-looking 300-KHz and a downward-looking 75-KHz ADCP, sampling depth ranges of 12–80 m and 100–800 m, respectively. Below the subsurface float, a McLane moored profiler (MP) measured profiles of temperature, salinity, and velocity from 90 to 1550 m. Deeper velocities were obtained with additional ADCPs at 1600 and 2600 m. On MPS, the MP sampled to 1265 m, and deeper velocity was measured with a 75-KHz ADCP sampling from about 1300- to 1600-m depths. All ADCPs sampled every 5 min, whereas the MPs completed an up or down profile each 1.25–1.5 h.

Strong tidal and mesoscale flows led to significant knock down of the mooring (up to 150 m), leading to two types of gaps in the record (Figs. 3b,c). The upper gaps occurred when the subsurface float was swept deep enough that the upper ADCP did not reach the surface. The maximum tilt of the subsurface float was 6°–8°, which is easily small enough for correction of the ADCP velocities. However, the mooring's tilt into the flow prevented the MP from being able to profile during these times, a well-known limitation of the instrument. These led to gaps in deep velocity (white spaces from 900 to 1580 m), primarily during the strongest westward flows. The gaps do not extend above 800–850 m, because the 75-KHz ADCP data are used there. Knockdowns at MPS were much less severe (50–60 m; not shown), presumably because it was situated outside of the Kuroshio.

The depth coverage from both moorings is incomplete and temporally variable, making it impossible to accurately compute baroclinic pressure because the depth integral of the isopycnal displacements is not known accurately. Hence, moored energy (Fig. 3d) and energy flux

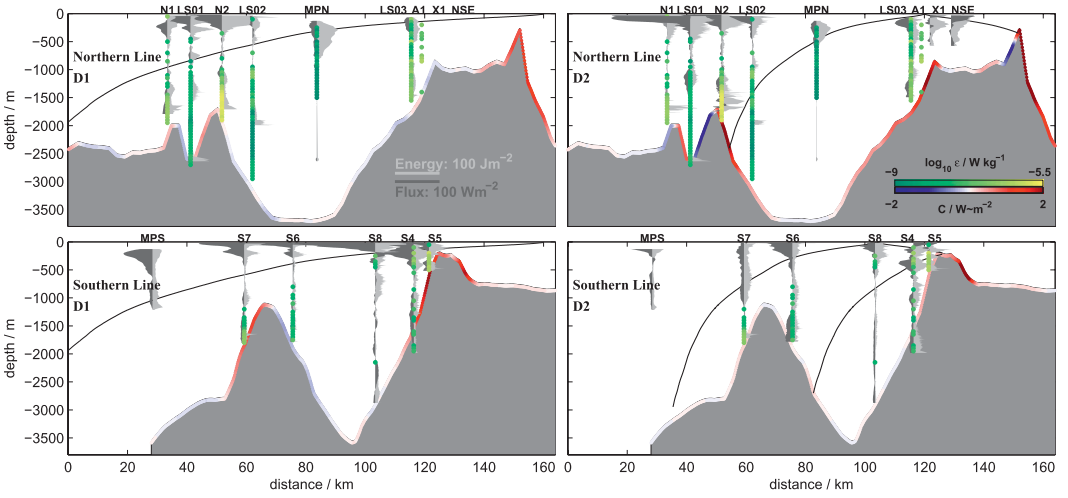

FIG. 2. Bathymetry and measured energy flux (dark gray), energy (light gray), and dissipation (colors) for each constituent along each line. Cross sections of model bathymetry (gray shading) and conversion (red–blue) are plotted along (top) the northern line and (bottom) the southern line, plotted vs distance from the western end of each line (see Fig. 1): (left) diurnal and (right) semidiurnal components. Characteristics computed from the measured stratification are indicated in each panel. At each station, along-line synoptic energy flux profiles are plotted in dark gray, with energy plotted as lighter gray, increasing to the right. Reference bars are shown in the top left panel. Time-mean dissipation rate for each station is plotted in green–yellow at each location (color scale in the top right panel).

(Fig. 3e) are computed as the sum of fits to the first three baroclinic modes, following standard techniques described in Nash et al. (2005). Depth profiles of energy flux are also computed for the depth range covered by the MP by using the sum of the first three modes to ensure that the depth-integrated baroclinic pressure is equal to zero, following Rainville and Pinkel (2006).

Because our measurements took place at different times of the diurnal and semidiurnal spring/neap cycles, an attempt was made to index calculated energy fluxes to the time mean over a fortnightly cycle by assuming that $F \sim u_{\mathrm{BT}}^2$, as expected (St. Laurent and Garrett 2002). The moored fluxes show this dependence on the upswing but fall off more quickly than the barotropic currents do (Fig. 3e), giving a lower power law when the whole record is used (upper inset). For each constituent, ''synoptic'' flux is computed as $F_s = F_{\mathrm{obs}}(t)[U_{\mathrm{BT}}(t)/U_{\mathrm{BT}}^{\mathrm{ref}}]^2$, where F_{obs} is the observed mean flux at each station. Here, $U_{\mathrm{BT}}(t)$ is the amplitude of the barotropic tidal velocity from TPXO6.2 (Fig. 3a, blue and red) and $U_{\mathrm{BT}}^{\mathrm{ref}}$ is the RMS amplitude of that constituent over the entire period. Because we seek a correction factor at each location and barotropic forcing does not vary greatly over our region, it is sufficient to use $U_{\mathrm{BT}}(t)$ from a single location to index each station (rather than needing to adjust it for local depth). Here, $U_{\mathrm{BT}}^{\mathrm{ref}} = 21.1$ and 14.9 cm s^{-1} for the diurnal and semidiurnal bands, respectively.

The raw and synoptic depth-integrated fluxes for each component are given in Table 1. Generally, the correction helps collapse flux data measured at different times in the cycle (e.g., semidiurnal fluxes at S6a and S6b). Synoptic fluxes are then overplotted in the respective panels of Fig. 1. Note that D_1 synoptic flux is not computed for stations sampled near the diurnal neap tide to avoid spuriously boosting weak signals. Hence, there are fewer values for D_1 than for D_2.

3. Model description

We use the Hallberg Isopycnal Model (Hallberg and Rhines 1996; Hallberg 1997), configured as an internal tide model as described by Simmons et al. (2004b), to predict the barotropic and baroclinic tides in the domain from 15 August to 14 September 2010. Bathymetry is 1/80°, obtained by subsampling the 30 arc-second Smith and Sandwell (1997) bathymetry using a nearest-neighbor scheme, with no smoothing. The model domain extends from 17° to 25°N and from 115° to 127.5°E. Model stratification is horizontally uniform, obtained from the Generalized Digital Environmental Model database (GDEM) climatology for the month of August (Teague et al. 1990), at the location nearest to our station S8. The model's 40 layers are distributed to optimally resolve the first baroclinic mode structure. Information on the subgrid-scale parameterization of viscosity and a description of the conversion and energy flux diagnostics for this model can be found in Simmons et al. (2004b).

The model is forced at the boundaries with current and elevation predictions for the M_2, S_2, O_2, and K_1 tidal constituents using TPXO6.2. Flatter open boundary

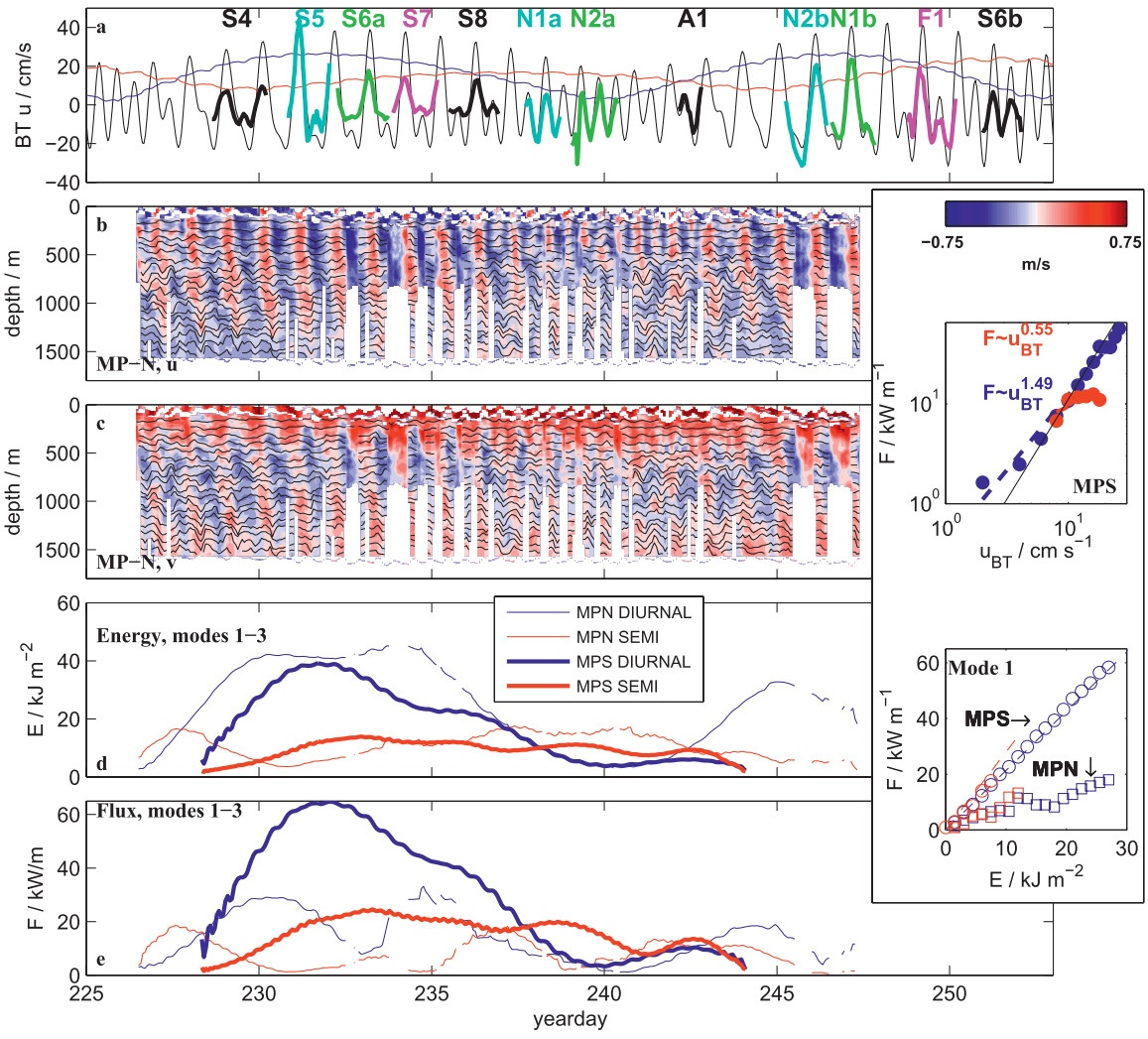

FIG. 3. Time series during the long cruise. (a) Barotropic tide predictions from TPXO6.2 evaluated at 20.6°N, 121.9°E (black), and measured depth-average velocity at each station. Station names are indicated at top. Blue and red curves are semidiurnal and semidiurnal amplitude computed in sliding 3-day windows. (b) Zonal and (c) meridional velocity, measured in the upper 1600 m at MPN. Isopycnals with 50-m mean spacing are overplotted. Gaps result from mooring knockdown (see text). (d) Depth-integrated energy at each mooring (diurnal is blue and semidiurnal is red). Moored energy is computed as the kinetic plus available potential energy summed over modes 1–3. (e) As in (d), but for flux magnitude. Inset gives (top) flux magnitude in each band plotted vs barotropic speed predicted from TPXO6.2 for each constituent, and (bottom) mode-1 flux magnitude plotted versus mode-1 energy. Circles and squares are from MPN and MPS, respectively, whereas dashed lines are predictions for a mode-1 wave traveling at the theoretical mode-1 group speed. Blue and red indicate diurnal and semidiurnal bands, as in the other panels.

conditions (Marchesiello et al. 2001) allow barotropic tidal energy to exit the domain. A viscous sponge layer damps internal tides as they approach the boundary by linearly increasing horizontal viscosity by two orders of magnitude starting ½° from the boundary.

4. Results

a. Internal tide: Basic description

An energetic internal tide is observed at all stations. The dominant frequency, easily seen at the northern mooring (Figs. 3b,c), changes from diurnal to semidiurnal and back again, following the barotropic forcing (Fig. 3a). The full vigor of the tidal signals can be seen in most of the LADCP time series, a selection of which is presented in Fig. 4. The top two panels show two occupations of station N2, on the eastern flank of the western ridge on the northern line (Fig. 1), whereas the bottom two panels are from station S6, at the analogous location on the southern line. Baroclinic flows are strong at all stations, approaching 2 m s^{-1} at N2, and generally exceeding barotropic velocities (Fig. 3a) by factors of 3–10.

TABLE 1. Station information, depth-integrated dissipation, and measured and synoptic fluxes for each constituent. See Fig. 3a for the time of each station. Stations A1 and LS06 allowed calculation of total flux but were cut short after ≈12 h because of weather, preventing separation of D_2 and D_1. The synoptic correction does not change for the individual components but can slightly for the total because of the different contributions to the vector sum. Here, $U_{\mathrm{BT}}^{\mathrm{ref}} = 0.21$ m s^{-1} for D_1 and 0.15 m s^{-1} for D_2. Direction, θ, is measured in degrees counterclockwise from east.

			$\int_0^H \epsilon$	Total flux (kW m^{-2})				D_1 flux (kW m^{-2})			D_2 flux (kW m^{-2})		
				Measured		Synoptic		Measured		Synoptic	Measured		Synoptic
Station	Lat, lon	H (m)	(W m^{-2})	Direction	Magnitude	Direction	Magnitude	Direction	Magnitude	Magnitude	Direction	Magnitude	Magnitude
S4	19.32°N, 121.17°E	2030	0.073	121	36.3	129	29.3	111	29.1	26.4	169	4.2	12.6
S5	19.3°N, 121.21°E	540	0.196	177	9.2	185	5.9	170	8.8	5.6	246	0.8	1.6
S6a	19.55°N, 120.86°E	1820	0.013	154	364	153	21.1	161	14.8	10.5	148	14.8	18.3
S6b	19.55°N, 120.86°E	1820	0.028	148	39	—	—	187	3	—	138	41.1	16.7
S7	19.64°N, 120.73°E	1820	0.069	154	23.4	151	18.8	156	17.2	16.8	143	8.9	8.5
S8	194°N, 121.07°E	3000	0.019	120	13.4	122	18.2	129	9.3	15.4	113	11.8	9.7
F1	19.57°N, 121.41°E	1200	0.189	152	41.8	157	24	158	16.6	19.8	154	26.6	13.5
N1a	20.59°N, 120.84°E	1800	0.245	200	20.5	—	—	76	4.4	—	189	17.5	14
N1b	20.59°N, 120.85°E	1800	0.071	166	25.8	170	14.9	128	13.2	89	201	10.9	11.9
N2a	20.59°N, 121.02°E	1800	1.29	209	16	—	—	167	0.9	—	183	15.6	14.1
N2b	20.59°N, 121.02°E	1800	0.545	138	40.9	144	27.7	126	32.2	22.5	169	6.8	16.1
A1	20.61°N, 121.67°E	1500	0.166	298	14.1	—	—	—	—	—	—	—	—
X1	20.61°N, 121.69°E	1000	—	274	17.7	—	—	18	1.8	—	269	18.2	22.3
NSE	20.61°N, 121.76°E	1000	—	344	11.2	—	—	74	3	—	329	11.6	14.2
LS01	20.57°N, 120.92°E	2750	0.033	175	195	163	27.2	179	4.5	8.7	157	14.4	25.8
LS02	20.56°N, 121.12°E	3000	0.352	121	26.2	110	13.7	93	8.6	5.1	117	9.7	12.6
LS03	20.5°N, 121.63°E	1500	0.238	208	25.2	222	14	227	13.6	5.9	220	13.2	12.6
LS04	20.56°N, 121.64°E	1500	0.145	225	32.5	220	18.2	229	6.5	3.4	218	19	17.8
LS05	20.56°N, 121.67°E	1000	0.173	243	14.6	239	12.3	268	2.3	1.6	235	12.3	12.2
LS07	20.56°N, 121.63°E	2000	0.12	248	29.2	—	—	—	—	—	—	—	—
MPN	20.6°N, 121.33°E	3664	0.004	181	4.7	181	4	161	0.9	0.9	185	3.9	3.9
MPS	19.81°N, 120.5°E	3697	—	169	38.6	169	29.1	175	26	26	156	13	13

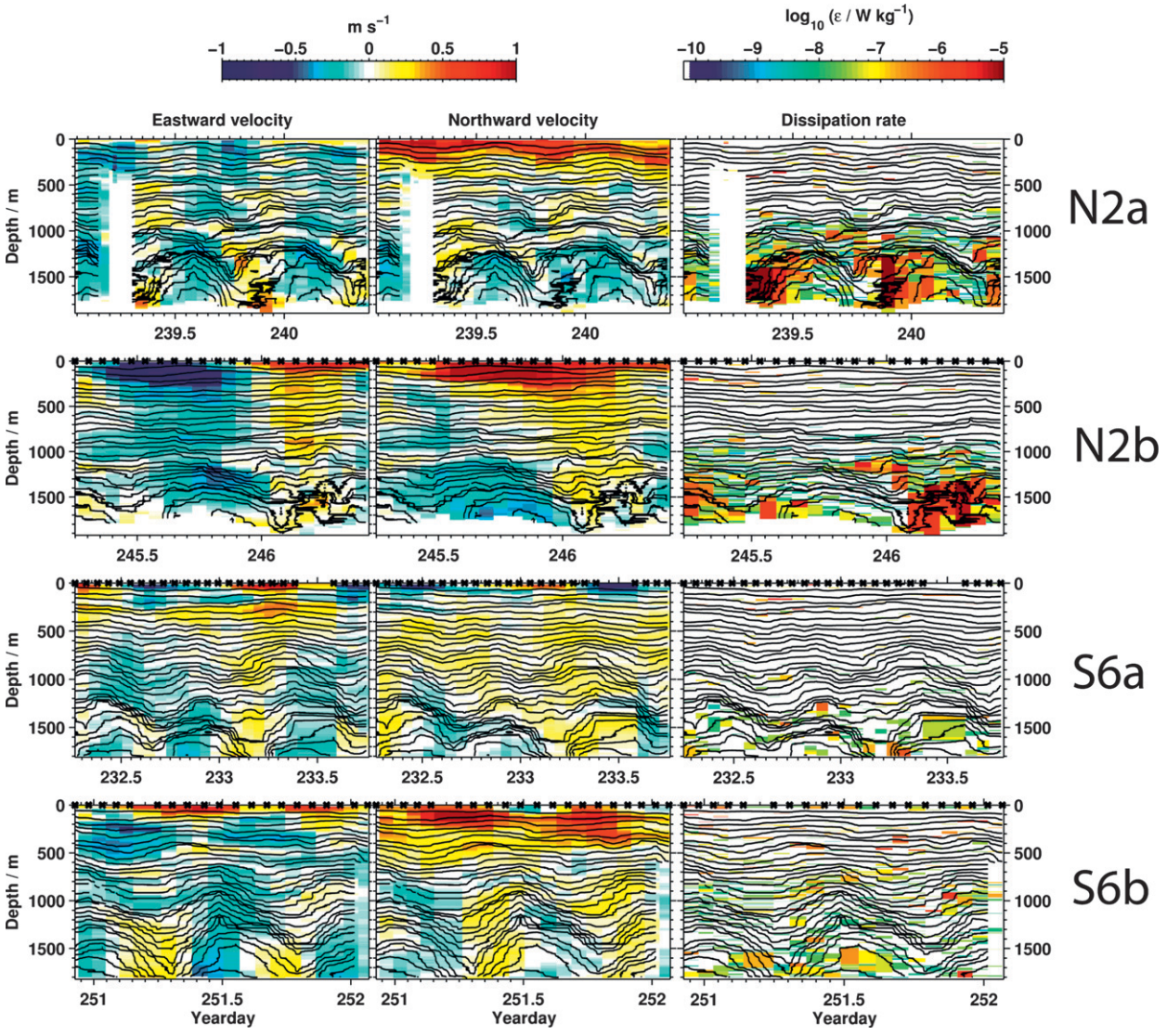

FIG. 4. Time series of (left) eastward and (middle) northward velocity and (right) Thorpe-inferred turbulent dissipation rate for stations (top to bottom) N2a, N2b, S6a, and S6b. Superimposed are density contours (black lines) that are evenly spaced in the resting depth of each isopycnal.

At all stations, semidiurnal and diurnal motions dominate, with no strong inertial peak evident in either the station or the moored data. Isopycnal displacements (black lines) are 300 m from peak to peak or greater at nearly all sites sampled, with maxima generally in the bottom few hundred meters. The associated baroclinic pressure anomaly is 1000 Pa, equivalent to a 10-cm deflection of the sea surface. The phasing between displacement and velocity is complicated, with some downward phase propagation seen (upward energy).

The Kuroshio is evident as a strong ($\approx$1 m s^{-1}) northward flow in the upper few hundred meters in both the northern mooring (Figs. 3b,c) and stations N2a and N2b but is absent in the southern stations. Regional satellite observations and models show that it meanders over a broad portion of Luzon Strait over a period of weeks (Caruso et al. 2006).

b. *Patterns of energy flux*

Patterns of observed energy flux, presented for each constituent in plan view in Fig. 1 and in cross section in Fig. 2 (dark gray profiles), are significantly different along the northern and southern lines. Along the southern line, flux in both diurnal and semidiurnal bands is westward at all stations. Flux in both bands is strongly surface intensified, consistent with dominantly mode-1 signals in strong stratification (Nash et al. 2005). An exception is station S6, where semidiurnal flux is intensified several

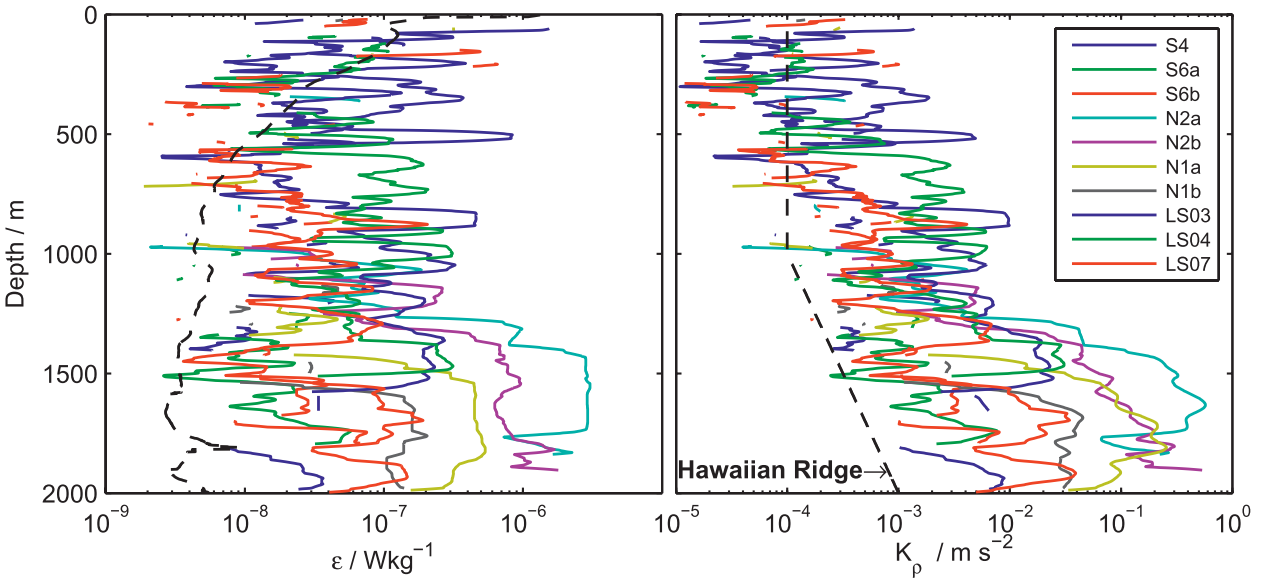

FIG. 5. Profiles of (left) dissipation rate and (right) diapycnal diffusivity at selected stations. The dashed line in the right panel is the fit for diffusivity by Klymak et al. (2006) to all profiles atop the Hawaiian Ridge. It is plotted as a dissipation rate as a dashed line in the left panel using the Luzon Strait stratification.

hundred meters above the bottom. Moored energy flux at MPS in each band (Fig. 3e) shows a spring–neap cycle generally in phase with forcing, though longer records are required for more certainty. Diurnal flux exceeds the semidiurnal by about a factor of 2.

Along the northern line, the depth-integrated flux is more dominantly semidiurnal, with a complicated spatial pattern. Flux vectors for both constituents swirl clockwise, with northward/southward fluxes over the western–eastern ridges. Between the ridges, measured and observed net flux is nearly zero, despite significant energy (Figs. 1, 2, light gray). These patterns, together with higher energy values in the middle, are clear signatures of an interference pattern from waves generated at the two ridges traveling in opposite directions (Nash et al. 2004), where rotation leads to correlations between transverse velocity and pressure. The resulting alternating bands of transverse energy flux give rise to the clockwise-swirling vectors.

The model conversion (Figs. 1, 2, red and blue) supports this interpretation, showing generation on the eastern flank of the western ridge along the northern line but not on the southern line. Semidiurnal flux at the easternmost stations turns eastward, which is consistent with the modeled semidiurnal conversion just west of there. In like manner, westward flux increases from station LS02 to N2, consistent again with strong generation just to the east. Note that this conversion does not generate westward signals; rather, the westward net flux increases because the stations are west of the eastward signals generated at 60 km.

To demonstrate the presence of the interference pattern at the northern ridge quantitatively, flux magnitude F is plotted versus energy E for mode 1 (Fig. 3, inset) and compared to the theoretical mode-1 group speed c_g. For free waves, F plotted versus E falls along a line of slope c_g (dashed), as observed at many moorings in the open ocean (Alford et al. 2006b; Alford and Zhao 2007). This behavior is observed at MPS (circles), as expected given its location west of both ridges. However, F/E is about 4 times smaller at MPN for both constituents (squares), indicating interference between signals from the two ridges.

As with the southern line, fluxes are mostly surface intensified. The exception is a deep westward flux at station N2a, approximately where expected for semidiurnal radiation generated at the eastern flank of the eastern ridge and reflected from the surface (Fig. 2, dark gray ray). This station is analogous to station S6a on the southern line (eastern side of the western ridge), where deep fluxes were also observed, although no such clear ray-path explanation is apparent for the southern station.

At all stations, observed depth-integrated fluxes are in remarkably good agreement with the modeled fluxes (Fig. 1). Exceptions include significantly stronger D_1 flux observed at the western end of the northern line (station N2b) and somewhat stronger D_2 fluxes observed on the southern line.

c. Dissipation

Turbulent dissipation rate is strongly tidally modulated at all stations, as shown at the right in Fig. 4. For

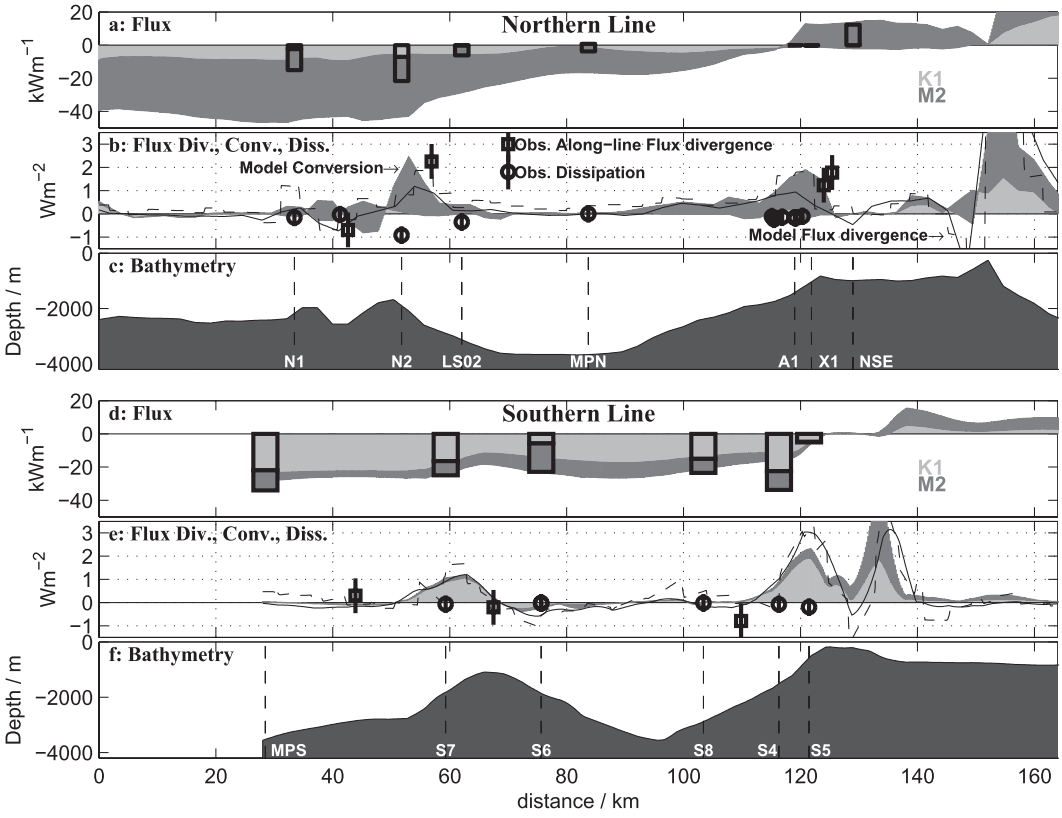

FIG. 6. Along-line synoptic energy flux in the diurnal and semidiurnal bands (light and dark gray), for (a) the northern line and (d) the southern line. Values are plotted as stacked histograms, with continuous traces and vertical bars showing model and observations, respectively. (b),(e) Model conversion in each band (light and dark gray) and model flux divergence (2D, $\nabla \cdot F$, is thin black and along line is dashed). Observed depth-integrated dissipation rate (circles) and flux divergence computed from adjacent station pairs (squares) are overplotted. Vertical lines indicate error bars. (c),(f) Bathymetry and station locations for each line are given.

example, the largest overturns at station N2, over 300 m high, occurred following the greatest downward displacements for both diurnal and semidiurnal periods. At S6, the same pattern is seen for the semidiurnal period. However, observed dissipation at S6 remains semidiurnal even during the diurnal period, showing two maxima during the record: one during downward isopycnals and one at maximum upward displacement. Although it seems clear that some form of convective instability or internal hydraulic phenomenon leads to the breaking, ongoing work seeks to determine the specific mechanisms, which likely depend on the location. For example, two-dimensional (2D) numerical simulations with the Massachusetts Institute of Technology general circulation model (MITgcm) give similar magnitude and phasing at station N2 to the observations but poorer agreement at other locations, possibly implicating three-dimensional processes. Preliminary indications (M. Buijsman 2010, personal communication) are that the ability of three-dimensional flows to go around rather than having to go over topographic features (as they do in 2D) leads to substantial differences.

Station-mean profiles of dissipation rate and diffusivity at all 2000-m stations (Fig. 5, with depth-integrated dissipation given in Table 1) were some of the largest ever observed. Turbulence was elevated in the bottom 500–1000 m at all stations, similar to the fit by Klymak et al. (2006) to data collected atop the Hawaiian Ridge (dashed). However, the Luzon Strait values in this depth range exceed those at the Hawaiian Ridge data by factors of 3–500. In particular, at the northern part of the western ridge, diffusivities on both flanks exceeded 10^{-1} m^2 s^{-1}, over 10 000 times typical open ocean values of $\approx 10^{-5}$ m^2 s^{-1} (Gregg 1989) and strong enough to erode stratification over 500-m vertical scales in only a few days. The mixed fluid is presumably replaced by the $\approx$1–2 Sv (1 Sv $\equiv 10^6$ m^3 s^{-1}) of deep water entering the South China Sea from the Pacific through Luzon Strait (Tian et al. 2010, manuscript submitted to *Nature*). Mixing likely plays a central role in modifying these waters, as suggested by Qu et al. (2006).

The spatial dependence of the measured dissipation is shown in Fig. 2 (colored profiles). Although a bias in the

stations chosen cannot be ruled out, observed turbulence at the northern-line stations was generally much stronger than along the southern line, despite comparable baroclinic energy levels (light gray). Station N2 showed by far the strongest turbulence, with depth-integrated dissipation values of 0.5 and 1.29 W m^{-2} for the two occupations (Table 1), followed by N1. These exceeded the corresponding values at S6 and S7 (the analogous southern stations on the western ridge) by factors of 25–50, in spite of similarly energetic flows there. The weakest northern-line value exceeded all southern values but S5, an active site in 500 m of water.

d. Energy budget

Internal tides in steady state should obey the energy equation

$$C - \nabla \cdot F = D, \tag{1}$$

where $C = U_{BT} \cdot \nabla H p_{bot}$ is the linear conversion (e.g., Kelly et al. 2010 and D represents all processes removing energy from the internal tide including dissipation and nonlinear energy transfers (of which we only measure the former). The model and observations are employed to investigate the observed and model energy balance according to (1) along each line. Flux is first plotted (Figs. 6a,d), again indicating an encouraging general agreement between observations and model.

Model flux divergence is examined next, summed over the D_1 and D_2 bands. Two-dimensional flux divergence (black) and along-line flux divergence (dashed) are similar, quantitatively expressing the visual conclusion from Fig. 1 that most flux is along line, with off-axis divergence playing a mostly minor role. Wherever possible, along-line flux divergence was also estimated from adjacent station pairs (squares). Though agreement is clearly not as good for the divergence as for the flux itself, the observed along-line flux divergence is large on the eastern flank of both ridges on the northern line, generally the same location and similar magnitude as the along-line model divergences.

Model conversion, plotted as the stacked linear sum of the D_1 and D_2 components (Figs. 6b,e, light and dark gray), balances the model flux divergence at many locations, particularly along the southern line. By (1), model dissipation therefore apparently plays a minor role at these locations. Agreement on the northern line is poorer, particularly near the western ridge, potentially suggesting a greater role for dissipation there. In support of these interpretations, observed depth-integrated dissipation from Table 1 (circles) is generally 1–2 orders of magnitude smaller than conversion and flux divergence at most stations. However, at N2, observed dissipation is of the same order of magnitude as the other quantities, at the location where their disagreement is greatest. Though these calculations fall far short of balancing an energy budget, they suggest that dissipation resulting from breaking near N2, which the model likely resolves poorly or not at all, are zero-order terms in the energy budget. It is possible that the interplay at that location between the incident westbound wave and the conversion leading to the eastbound wave may lead to the large dissipations, which in turn could affect the generation process.

5. Summary and discussion

This paper has presented some of the first observations of energy flux and turbulence in Luzon Strait, a complicated double-ridge system between Taiwan and the Philippines. Data were collected along two lines: one where the interridge spacing is close to a semidiurnal wavelength—giving rise to the possibility of resonance as suggested by Echeverri and Peacock (2010)—and one along a southern line, where the spacing should be nonresonant. Internal tide energy, energy flux, and dissipation rate are all extremely high at all sites by open ocean standards and even relative to strong single-ridge generation sites such as the Hawaiian Ridge. At the site of strongest dissipation, dissipation and diffusivity exceed 2×10^{-6} W kg^{-1} and 0.2 m^2 s^{-1}, respectively, which is large enough to represent significant loss terms in the energy balance.

Though the model likely does not represent dissipative processes correctly, it is tempting to take advantage of the general agreement between the observed and modeled fluxes to use (1) to obtain a simple estimate of q. We do this by simply integrating model conversion in both semidiurnal and diurnal bands over the region shown in Fig. 1 (obtaining 24.1 GW) and by comparing it to the total flux radiated out the sides of the domain: 7.89, 6.05, 0.16, and 0.47 GW are radiated out the western, eastern, southern, and northern sides, respectively, for a total of 14.57 GW. Therefore, 9.5 GW is dissipated within the domain, giving $q = 0.39$. Compared to estimates at the Hawaiian Ridge from observations (Klymak et al. 2006; $q = 0.08$–0.25) and Princeton Ocean Model simulations (Carter et al. 2008; $q = 0.19$), the Luzon Strait appears more fractionally dissipative, possibly because of the more nonlinear internal tides and/or the second ridge. More modeling and observations are necessary to confirm or deny this speculation.

Interference patterns observed along the northern line but not the southern line are as expected, given conversion from the model, confirming the importance of the western ridge and its spacing from the eastern one in setting the patterns of energy flux. Although more detailed modeling is required for certainty, we tentatively

suggest that at least part of the strength of the internal tides and their dissipation owes to the interaction between signals generated at the two ridges. Consistent with the general ideas of resonance, stronger dissipation is observed along the northern line, where the ridge spacing is correct for semidiurnal signals generated at the eastern ridge to interact strongly with the western ridge and enhance conversion there (as seen by the characteristics in Fig. 2, top right).

Not all of our data are consistent with this notion, however. For example, dissipation is elevated at N2 during both semidiurnal and diurnal periods. However, resonance would only be expected for semidiurnal motions (Fig. 2). Is a different mechanism or an interaction between the two frequencies responsible for the diurnal dissipations? Ongoing work seeks to determine the cause of these strong dissipations, as well as their dependence on other time-dependent factors such as the Kuroshio and seasonal modulation of the stratification.

Acknowledgments. This work was supported by the Office of Naval Research under Grants N00014-09-1-021, N00014-09-1-0273, N00014-09-1-0281, and N00014-09-1-0274. We are grateful to our Taiwanese colleagues David Tang, Y.-J. Yang, and Yu-Huai Wang for their assistance in logistics; to John Mickett, Mike Carpenter, and Zoë Parsons for their hard work and skill in preparing and deploying the moorings; and to captain Dave Murline and the crew of R/V *Revelle* for their seamanship and can-do attitude.

REFERENCES

Alford, M. H., and Z. Zhao, 2007: Global patterns of low-mode internal-wave propagation. Part II: Group velocity. *J. Phys. Oceanogr.,* **37,** 1849–1858.

——, D. W. Gerdt, and C. M. Adkins, 2006a: An ocean refractometer: Resolving millimeter-scale turbulent density fluctuations via the refractive index. *J. Atmos. Oceanic Technol.,* **23,** 121–137.

——, M. C. Gregg, and M. A. Merrifield, 2006b: Structure, propagation, and mixing of energetic baroclinic tides in Mamala Bay, Oahu, Hawaii. *J. Phys. Oceanogr.,* **36,** 997–1018.

——, R. Lien, H. Simmons, J. M. Klymak, Y. Yang, D. Tang, and M. Huei Chang, 2010: Speed and evolution of nonlinear internal waves transiting the South China Sea. *J. Phys. Oceanogr.,* **40,** 1338–1355.

Althaus, A., E. Kunze, and T. Sanford, 2003: Internal tide radiation from Mendocino Escarpment. *J. Phys. Oceanogr.,* **33,** 1510–1527.

Carter, G. S., and Coauthors, 2008: Energetics of M_2 barotropic-to-baroclinic tidal conversion at the Hawaiian Islands. *J. Phys. Oceanogr.,* **38,** 2205–2223.

Caruso, M. J., G. G. Gawarkiewicz, and R. C. Beardsley, 2006: Interannual variability of the Kuroshio intrusion in the South China Sea. *Oceanography,* **62,** 559–575.

Cole, S. T., D. L. Rudnick, B. A. Hodges, and J. P. Martin, 2009: Observations of tidal internal wave beams at Kauai Channel, Hawaii. *J. Phys. Oceanogr.,* **39,** 421–436.

Dillon, T. M., 1982: Vertical overturns: A comparison of Thorpe and Ozmidov length scales. *J. Geophys. Res.,* **87,** 9601–9613.

Echeverri, P., and T. Peacock, 2010: Internal tide generation by arbitrary two-dimensional topography. *J. Fluid Mech.,* **659,** 247–266.

Egbert, G., and S. Erofeeva, 2002: Efficient inverse modeling of barotropic ocean tides. *J. Atmos. Oceanic Technol.,* **19,** 183–204.

Ferron, B. H., H. Mercier, K. Speer, A. Gargett, and K. Polzin, 1998: Mixing in the Romanche Fracture Zone. *J. Phys. Oceanogr.,* **28,** 1929–1945.

Gregg, M., 1989: Scaling turbulent dissipation in the thermocline. *J. Geophys. Res.,* **94,** 9686–9698.

Hallberg, R., 1997: Stable split time stepping schemes for large-scale ocean modeling. *J. Comput. Phys.,* **135,** 54–65.

——, and P. Rhines, 1996: Buoyancy-driven circulation in an ocean basin with isopycnals intersecting the sloping boundary. *J. Phys. Oceanogr.,* **26,** 914–940.

Kelly, S. M., and J. D. Nash, 2010: Internal-tide generation and destruction by shoaling internal tides. *Geophys. Res. Lett.,* **37,** L23611, doi:10.1029/2010GL045598.

——, ——, and E. Kunze, 2010: Internal-tide energy over topography. *J. Geophys. Res.,* **115,** C06014, doi:10.1029/2009JC005618.

Klymak, J. M., and S. Legg, 2010: A simple mixing scheme for models that resolve breaking internal waves. *Ocean Modell.,* **33,** 224–234.

——, and Coauthors, 2006: An estimate of tidal energy lost to turbulence at the Hawaiian Ridge. *J. Phys. Oceanogr.,* **36,** 1148–1164.

——, R. Pinkel, and L. Rainville, 2008: Direct breaking of the internal tide near topography: Kaena Ridge, Hawaii. *J. Phys. Oceanogr.,* **38,** 380–399.

——, M. H. Alford, R. Pinkel, R. C. Lien, and Y. J. Yang, 2011: The breaking and scattering of the internal tide on a continental slope. *J. Phys. Oceanogr.,* **41,** 926–945.

Marchesiello, P., J. C. McWilliams, and A. Shchepetkin, 2001: Open boundary conditions for long-term integration of regional oceanic models. *Ocean Modell.,* **3,** 1–20.

Nash, J. D., E. Kunze, J. M. Toole, and R. W. Schmitt, 2004: Internal tide reflection and turbulent mixing on the continental slope. *J. Phys. Oceanogr.,* **34,** 1117–1134.

——, M. H. Alford, and E. Kunze, 2005: Estimating internal-wave energy fluxes in the ocean. *J. Atmos. Oceanic Technol.,* **22,** 1551–1570.

Nikurashin, M., and S. Legg, 2011: A mechanism for local dissipation of internal tides generated at rough topography. *J. Phys. Oceanogr.,* **41,** 378–395.

Osborn, T. R., 1980: Estimates of the local rate of vertical diffusion from dissipation measurements. *J. Phys. Oceanogr.,* **10,** 83–89.

Polzin, K., 2004: Idealized solutions for the energy balance of the finescale internal wave field. *J. Phys. Oceanogr.,* **34,** 231–246.

Qu, T., Y. Du, and H. Sasaki, 2006: South China Sea throughflow: A heat and freshwater conveyor. *Geophys. Res. Lett.,* **33,** L23617, doi:10.1029/2006GL028350.

Rainville, L., and R. Pinkel, 2006: Baroclinic energy flux at the Hawaiian ridge: Observations from the R/P *FLIP*. *J. Phys. Oceanogr.,* **36,** 1104–1122.

——, T. M. S. Johnston, G. S. Carter, M. A. Merrifield, R. Pinkel, B. D. Dushaw, and P. Worcester, 2010: Interference pattern and propagation of the M_2 internal tide south of the Hawaiian Ridge. *J. Phys. Oceanogr.,* **40,** 311–325.

Ramp, S. R., Y. Yang, and F. L. Bahr, 2010: Characterizing the nonlinear internal wave climate in the northeastern South China Sea. *Nonlinear Processes Geophys.,* **17,** 481–498.

Simmons, H., R. Hallberg, and B. Arbic, 2004a: Internal wave generation in a global baroclinic tide model. *Deep-Sea Res. II,* **51,** 3043–3068.

——, S. Jayne, L. S. Laurent, and A. Weaver, 2004b: Tidally driven mixing in a numerical model of the ocean general circulation. *Ocean Modell.,* **82,** 245–263.

Smith, W. H., and D. T. Sandwell, 1997: Global sea floor topography from satellite altimetry and ship depth soundings. *Science,* **277,** 1956–1962.

St. Laurent, L., and C. Garrett, 2002: The role of internal tides in mixing the deep ocean. *J. Phys. Oceanogr.,* **32,** 2882–2899.

Tang, W., and T. Peacock, 2010: Lagrangian coherent structures and internal wave attractors. *Chaos,* **20,** 017508, doi:10.1063/1.3273054.

Teague, W. J., M. J. Carron, and P. J. Hogan, 1990: A comparison between the generalized Digital Environmental Model and Levitus climatologies. *J. Geophys. Res.,* **95,** 7167–7183.

Thorpe, S., 1977: Turbulence and mixing in a Scottish loch. *Philos. Trans. Roy. Soc. London,* **286A,** 125–181.

Thurnherr, A. M., 2010: A practical assessment of the errors associated with full-depth LADCP profiles obtained using Teledyne/RDI Workhorse acoustic Doppler current profilers. *J. Atmos. Oceanic Technol.,* **27,** 1215–1227.

Zhao, Z., M. H. Alford, J. A. MacKinnon, and R. Pinkel, 2010: Long-range propagation of the semidiurnal internal tide from the Hawaiian Ridge. *J. Phys. Oceanogr.,* **40,** 713–736.